THE JOURNAL OF PHYSICAL CHEMISTRY C

Article

pubs.acs.org/JPCC

Doping the Superatom with p-Elements: The Role of p-Block Endohedral Atoms in Bonding and Optical Properties of E@$Au_{24}(SR)_{18}$ (E = Si, Ge, Sn, and Pb) from Relativistic DFT Calculations

Johanna Camacho Gonzalez[†] and Alvaro Muñoz-Castro*[,‡,§]

[†]Facultad de Filosofía y Humanidades, Universidad de Chile, Avenida Capitán Ignacio Carrera Pinto 1025, Ñuñoa, Santiago 7800284, Chile

[‡]Grupo de Química Inorgánica y Materiales Moleculares, Universidad Autonoma de Chile, El Llano Subercaseaux 2801, Santiago 8910060, Chile

[§]Doctorado en Fisico Quimica Molecular, Universidad Andres Bello, Avenida Republica 275, Santiago 8370146, Chile

Supporting Information

ABSTRACT: Expanding the versatility of well-defined clusters seeking distinctive physical and chemical behavior in a rational manner is a relevant issue in the design of functional nanostructures. Superatomic clusters through the prominent $Au_{25}(SR)_{18}$ aggregate offer an ideal template and robust framework to gain understading of the different behavior gained by the inclusion of different endohedral dopant atoms. Our results allow to gain more insights into the role of group XIV elements for both optical and bonding, revealing characteristic patterns to be expected in their low-energy UV-spectrum. The bonding shows an extension of the regular s-type interaction observed in $[Au@Au_{24}(SR)_{18}]^-$ to a more extended and covalent interaction given by s- and p-type interaction when the central atom is replaced by a group XIV elements, which can be expected of other endohedral p-block elements. In addition, the role of the spin−orbit coupling into the electronic and optical properties is discussed in terms of the new selection rules required by such regime. The characteristic optical and bonding patterns resulting from the p-element endohedral doping of the $Au_{25}(SR)_{18}$ superatom shed light into the rational variation of the molecular properties upon inclusion of an endohedral p-block element.

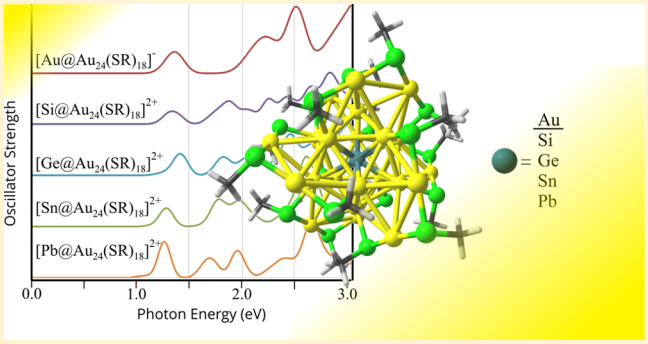

INTRODUCTION

The considerable interest in gold nanostructures is driven by the fact that these aggregates can serve as efficient building blocks for functional nanomaterials displaying unique physical and chemical behavior.[1−10] Their novel properties lead to promising applications in catalysis, sensing, and biomedicine among others.[9−16] Efforts on the understanding of stable gold clusters have been devoted to the rationalization of their structural and electronic properties, where numerous theoretical and experimental[17−23] efforts seek the obtention of novel displaying special electronic, optical, and structural properties.

For the last decades, development of synthetic strategies for ligand-protected (LP) gold clusters has led to a plethora of interesting structures,[18,23] reaching atomically precise sizes. Such systems are generally composed by a finite number of atoms exhibiting a discrete electronic structure resulting from the inner metallic core protected by several stabilizing groups such as thiolate and phosphine ligands or capping metallic aggregates, among others.[6,24−26] In particular, thiolate-protected gold nanoclusters have been extensively developed owing to the resulting strong gold−gold and gold−sulfur interactions, which yield structures that are stable against degradation.[5,27−30] The stability of the overall cluster originates from the electronic and structural states of the metallic core with a magic number of valence electrons (ve) according to the superatom concept.[6,17,31−33]

$Au_{25}(SR)_{18}$ is one of the most prominent members displaying a high stability owing to both geometric and electronic factors. X-ray crystallography has shown an icosahedral Au_{13} core surrounded by a protecting layer composed by six dimeric $Au_3(SR)_2$ staple units.[5] The central core is formed by an endohedral gold atom embedded into a deltahedral Au_{12} cage, formally displaying 8-ve according to the electron count rules given by Häkkinen and co-workers.[6,17]

Received: May 16, 2016
Revised: November 3, 2016
Published: November 4, 2016

DOI: 10.1021/acs.jpcc.6b04943
J. Phys. Chem. C 2016, 120, 27019−27026

Table 1. Selected Geometrical Parameters, CShM Values in Relation to a Perfect Icosahedral Au_{12} Cage, Charge Analysis (Hirshfeld) for the Endohedral Element (E), for the Inner Core ($E@Au_{12}$), and the Protecting Layer (PL), HOMO−LUMO Gap, and Contribution from the Endohedral Atom (E) to Frontier Orbitals

			CShM	charge					
	$R.Au_{12}$Cage	$R.Au_{12}$Out	cage	E	$E@Au_{12}$	PL	H−L gap	%E HOMO	%E LUMO
$[Au_{24}(SMe)_{18}]^{2-}$	2.773	5.141	0.17		0.11	−2.11			
$[Au@Au_{24}(SMe)_{18}]^{-}$	2.854	5.106	0.12	0.01	0.22	−1.22	1.205	14.7%	5.4%
$[Si@Au_{24}(SMe)_{18}]^{2+}$	2.839	5.129	1.90	−0.15	0.74	1.26	1.135	8.8%	0.0%
$[Ge@Au_{24}(SMe)_{18}]^{2+}$	2.858	5.072	0.33	−0.10	0.81	1.19	1.135	12.1%	6.0%
$[Sn@Au_{24}(SMe)_{18}]^{2+}$	2.928	5.094	0.87	−0.09	0.69	1.31	1.048	16.1%	4.1%
$[Pb@Au_{24}(SMe)_{18}]^{2+}$	3.012	5.096	1.02	−0.05	0.63	1.37	0.968	22.7%	11.5%

These 8-ve fulfill the closure of s and p superatomic electronic shells, reaching a $1s^21p^6$ electronic configuration with exceptional stability in its anionic $[Au_{25}(SR)_{18}]^-$ form. Therefore, such superatoms can be viewed as an analogous to noble gas atoms, being exceptionally stable owing to the shell-closing electron count.[34]

Optical properties of thiolate-protecting gold clusters have been explored in great detail, offering experimental evidence to characterize and distinguish between different gold clusters,[23] leading to promising applications as optical, chiroptical, photoluminescent molecular devices.[35] Such properties reflect the fascinating size-dependent behavior which originates from the inner metallic core embedded in the protecting layer. From the superatomic approach, the observed properties are nicely rationalized in terms of superatomic shells, which facilitate a deeper understanding and comparison along different gold nanoclusters[36] in nuclearity and shape.

The evaluation of stable gold clusters in relation to their structural and discrete electronic states,[6,18,21,22,37] has contributed largely to rationalize their behavior gaining a fundamental understanding of novel clusters displaying outstanding stability. In recent years, the inclusion of different atoms within the Au_{13} core has been studied as a useful strategy to expand the versatility of $[Au_{25}(SR)_{18}]^-$.[34,38−44] The effect of the dopant atom has been observed to increase the stability when the central gold atom is replaced by palladium and platinum,[39,44] with promising catalytic activities. Cd and Hg have been also explored, being located at the Au_{12} cage.[38]

By taking advantage of superatom concept, Jiang and co-workers explored several elements as endohedral atoms revealing a favorable aggregation, with a subsequent change in HOMO−LUMO gap.[34] Thus, the $M@Au_{24}(SR)_{18}$ template is a prototypical and robust framework to gain understading of the different behavior of the superatomic entity along different endohedral dopant atoms.

Here, inspired by the work of Jiang and co-workers,[34] we set to gain a deeper understanding of the optical and electronic properties variation by including group XIV elements (E = Si, Ge, Sn, and Pb) by using relativistic DFT methods. Preliminarly, it is expected that these endohedral elements expand the s-type concentric interaction observed in $Au@Au_{24}(SR)_{18}$, originated between the s-atomic shell of the inner atom and the Au_{12} cage, to both s- and p-type interactions, when such elements are involved.

COMPUTATIONAL DETAILS

Relativistic density functional theory calculations[45] were carried out by using the ADF code,[46] incorporating scalar (SR) and spin−orbit (SOC) corrections via the one- and two-component ZORA Hamiltonians,[47] respectively. We employed the triple-ξ Slater basis set, plus two polarization functions (STO-TZ2P) for valence electrons, within the generalized gradient approximation (GGA) according to the Perdew−Burke−Ernzerhof (PBE) exchange-correlation functional[48,49] because of its improved performance on long-range interactions and relatively low computational cost employed in similar clusters, allowing a direct comparisons with other computational studies of gold nanoclusters.[22,36,50−52] The frozen core approximation was applied to the $[1s^2−4f^{14}]$ shells for Au, $[1s^2−2p^6]$ for Si, $[1s^2−3d^{10}]$ for Ge, $[1s^2−4d^{10}]$ for Sn, $[1s^2−5d^{10}]$ for Pb, and $[1s^2]$ for C, leaving the remaining electrons to be treated variationally. Geometry optimizations were performed without any symmetry restrain, via the analytical energy gradient method implemented by Versluis and Ziegler.[53] An energy convergence criterion of 10^{-4} Hartree, gradient convergence criteria of 10^{-3} Hartree/Å and radial convergence criteria of 10^{-2} Å were employed for the evaluation of the relaxed structures. Deviations of selected fragments from a perfect icosahedron was evaluated by using the continuous-shape-measure (CShM) software by Alvarez and co-workers.[54−56]

RESULTS AND DISCUSSION

Selected average bond lengths and cage radii for the isoelectronic series involving the $[Au_{24}(SR)_{18}]^{2-}$ template, $[Au@Au_{24}(SR)_{18}]^-$, and $[E@Au_{24}(SR)_{18}]^{2+}$, with R = Me, are given in Table 1. The obtained structures (Figure 1) are in agreement to previous reports,[34] depicting a favorable incorporation for group XIV elements. In comparison to $[Au@Au_{24}(SMe)_{18}]^-$, the radius of the icosahedral Au_{12} cage decreases slightly for $[Si@Au_{24}(SMe)_{18}]^{2+}$, which then increases for Ge, Sn, and Pb clusters (Table 1). The endohedral carbon counterpart exhibits a larger distortion of the $C@Au_{12}$ core owing to its preference to generate endohedral $C@Au_5$ or $C@Au_6$ cores[57−60] (Supporting Information), leading to a larger destabilization of the $Au_{24}(SR)_{18}$ framework.[34] Hence, in

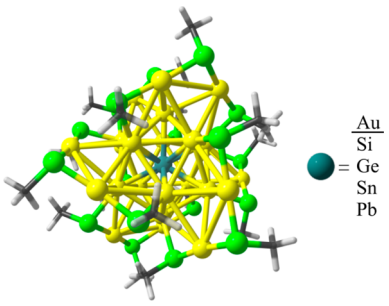

Figure 1. Structural representation of the isoelectronic $[Au@Au_{24}(SMe)_{18}]^-$ and $[E@Au_{24}(SMe)_{18}]^{2+}$ (E = Si, Ge, Sn, and Pb).

DOI: 10.1021/acs.jpcc.6b04943
J. Phys. Chem. C 2016, 120, 27019−27026

Table 2. Energy Decomposition Analysis for the Interaction Involving the Endohedral Atom and $[Au_{24}(SR)_{18}]^{2-}$[a]

@	Au		Si		Ge		Sn		Pb	
ΔE_{prep}	12.7		22.6		17.4		35.4		39.4	
ΔE_{orb}	−906.1	34.5%	−1675.5	75.9%	−1629.8	71.3%	−1390.3	66.9%	−1417.9	66.8%
ΔE_{elstat}	−1667.7	63.4%	−526.1	23.8%	−648.0	28.3%	−679.5	32.7%	−694.4	32.7%
ΔE_{pauli}	1181.9		89.7		80.4		127.8		124.9	
ΔE_{disp}	−55.5	2.1%	−6.7	0.3%	−7.88	0.3%	−9.9	0.5%	−11.5	0.5%
ΔE_{int}	−1447.5		−2118.6		−2205.3		−1951.9		−1998.8	

[a]Values in kcal·mol^{-1}.

the following, $[C@Au_{24}(SMe)_{18}]^{-}$ is not further discussed in order to focus on the $E@Au_{12}$ core based clusters given by the Si, Ge, Sn, and Pb series. Interestingly, different positions of the doping element appears as possible isomers of $[E@Au_{24}(SMe)_{18}]^{2+}$ which according to our preliminary calculations lie in a narrow range of 15 kcal·mol^{-1} for a dicationic singlet ground-state. This observation calls to an extended exploration of different overall charges and spin-multiplicity states in order to rationalize the mechanism underlying the preference for doping multiple sites in the $Au_{25}(SR)_{18}$ structure, followed by a detailed study as developed below for $[E@Au_{24}(SMe)_{18}]^{2+}$.

From Si to Pb, the $E@Au_{12}$ cage radius varies from 2.839 to 3.012 Å due to the increasing atomic radii for heavier counterparts. In contrast, the external gold atoms forming the protecting layer (staple gold atoms) trend to decrease its distance to the center showing a smaller radius for Ge, Sn, and Pb, in comparison to $[Au@Au_{24}(SMe)_{18}]^{-}$. The structural distortion from the relaxed geometry for the hollow $[Au_{24}(SR)_{18}]^{2-}$ template, accounts for the destabilization effect upon inclusion of the endohedral atoms, given by the preparation energy on Table 2. For $[Au@Au_{24}(SMe)_{18}]^{-}$, the structural changes leads to a destabilization of about 12.7 kcal·mol^{-1}. For silicon, the structural modification of the cage driven by the small atomic radius for silicon decreases the averaged Au_{12} cage radius from 2.854 to 2.839, in comparison to that of the gold counterpart. This results in a destabilization of about 22.6 kcal·mol^{-1}. In the endohedral germanium cluster, a destabilization of 17.4 kcal·mol^{-1} is obtained, which rises to 35.4 and 39.4 kcal·mol^{-1} for the Sn and Pb analogues, respectively.

In order to account for the structural modification required for allocate group XIV elements as an endohedral atom in the Au_{12} cage, we also employed the continuous-shape-measure (CShM) approach[54−56] developed by Alvarez and co-workers, to further quantify the departure from the icosahedral structure. The values of CShM (Table 1) are close to zero for a structure which is fully coincident with the reference polyhedron, an I_h polyhedra in our case, evolving to larger values when the structure is more distorted. For $[Au@Au_{24}(SMe)_{18}]^{-}$, the deviation of the Au_{12} cage from a perfect icosahedron is smaller in comparison to the hypothetical hollow $[Au_{24}(SMe)_{18}]^{2-}$ structure (CShM = 0.12 versus 0.17, respectively), suggesting that the inclusion of the endohedral gold atom favors a more symmetrical disposition of the cage gold atoms. The inclusion of Si leads to a larger distortion from the icosahedral symmetry, accounted for by the CShM = 1.89 parameter, which is reduced to CShM = 0.33 in the germanium counterpart. Then, the distortion increases slightly in Sn and Pb, with CShM values of 0.87 and 1.01 respectively. For comparison, the relaxed structure obtained for $[C@Au_{24}(SMe)_{18}]^{2+}$, exhibits the larger distortion (see above) from the expected icosahedral Au_{12} cage (CShM = 4.59) owing to its preference to form $C@Au_6$ cores as discussed above and showed in the Supporting Information. The involved preparation energy to form $[C@Au_{24}(SMe)_{18}]^{2+}$ amounts to 41.0 kcal mol^{-1}.

Atomic charges were obtained using the Hirshfeld charge analysis method[61,62] to estimate the charge distribution along the isoelectronic $[E@Au_{24}(SMe)_{18}]^{2+}$ clusters, in order to analyze the effect of the endohedral atom. The central $E@Au_{12}$ structure exhibits charges from 0.22 au for the Au counterpart, which becomes more positive for the group XIV elements. The difference in the overall charge from −1 to +2 in $[Au@Au_{24}(SMe)_{18}]^{-}$ and $[E@Au_{24}(SMe)_{18}]^{2+}$, respectively, is mostly accounted for by the variation of the electron charge in the staple motif layer. As a result, the ligand protected layer exhibits a charge of −1.22 au in the gold counterpart, which decreases to about +1.2 au for Si, Ge, Sn, and Pb systems. Interestingly, this behavior suggests that the inner core becomes more electron-acceptor going down in the group, attracting more charge from the external $Au_{12}(SMe)_{18}$ protecting layer.

In terms of the electronic structure, the variation from an endohedral Au atom to a group XIV element is schematically given in Figure 2. The superatom model[6,22,24,32] rationalize the particular stability of $[Au@Au_{24}(SMe)_{18}]^{-}$ in terms of the electronic shell-closing situation. Formally, the inner $Au@Au_{12}$ core exhibits 8 valence electrons according to the electron count rules given by Häkkinen and co-workers,[6] fulfilling the 1s and 1p superatomic shells in its $[Au@Au_{12}]^{5+}$ form. The LUMO is composed by the1d shell, which is split by symmetry in 2- and 3-fold levels. The 1f shell is given by a 3-fold level owing to group-theory reasons.[63] From Figure 2, the main bonding situation between Au and $Au_{24}@(SMe)_{18}$ is given by an s-type interaction involving both 6s-Au and 1s superatomic shell of $[Au_{24}(SMe)_{18}]$, leading to the overall 1s-$[Au_{25}(SMe)_{18}]$ shell of bonding character. In addition, the complementary antibonding 2s combination is also formed, which remain

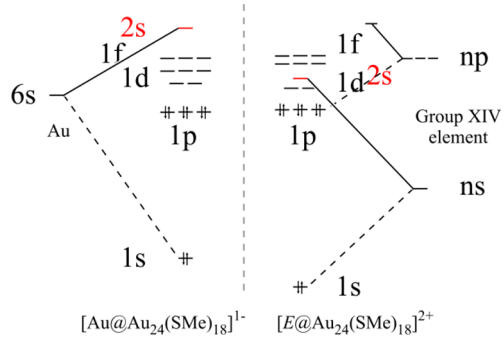

Figure 2. Schematic representation of the electronic structure for $[Au@Au_{24}(SMe)_{18}]^{-}$ and $[E@Au_{24}(SMe)_{18}]^{2+}$ (E = Si, Ge, Sn, and Pb), highlighting the endohedral atom interaction.

DOI: 10.1021/acs.jpcc.6b04943
J. Phys. Chem. C 2016, 120, 27019−27026

unoccupied above the superatomic 1d and the respective part of the 1f shell.

Similarly, the E@Au_{12} cores bear eight valence electrons in $[E@Au_{12}]^{8+}$ form, which is the driving factor for the positive charge in the protecting staple motif layer discussed above. Owing to the *n*s and *n*p atomic shells available for E elements, the bonding situation is given by both s- and p-type interactions in the 1s and 1p superatomic orbitals. A consequence of the inclusion of a more electronegative element, the s-shells are more stabilized resulting in a 1s shell with a lower energy, which in turn stabilizes the 2s shell now located between both 1d levels. Hence, the location of the 2s shell is the main difference between Au and E, in terms of electronic structure.

The variation of the electronic structure depicting the superatomic orbitals is given in Figure 3. The HOMO−LUMO

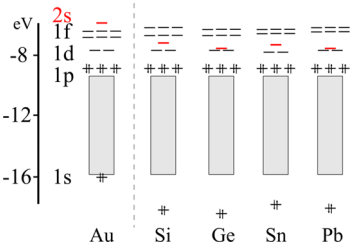

Figure 3. Electronic structure for the studied compounds at the scalar relativistic (SR) level of theory. Gray box depicts the "5d-block".

gap varies in agreement to the previous work of Jiang and co-workers,[34] showing a decrease from Si- to Pb-doped systems. The gap obtained for the silicon counterpart is smaller than that described for $[Au@Au_{24}(SMe)_{18}]^{-}$ amounting to 1.135 eV and is similar to that of the germanium endohedral structure. For Sn and Pb, such gap decreases to 1.048 and 0.968 eV, respectively, denoting the possibility of fine-tuning for the electronic structure in the studied isoelectronic series. The involved frontier orbital given by 1p and 1d superatomic shells, are composed in about 14.7 and 5.4% from the endohedral gold atom in $[Au@Au_{24}(SMe)_{18}]^{-}$. The contribution from the group XIV endohedral atom for the HOMO (1p), increases from 8.8 to 22.7%. Similarly, the LUMO (1d) exhibits an increasing character from the central atom going to 0.0 to 11.5%, going down in the group.

Thus, for the heavier counterpart, namely, $[Pb@Au_{24}(SMe)_{18}]^{2+}$, the HOMO and LUMO are contributed to in a larger amount by the endohedral atom, suggesting its larger influence in observable molecular properties involving frontier orbitals, such as optical and redox properties. Hence, in the $Au_{24}(SR)_{18}$ framework, a heavier doping central atom contributes involves a stronger p-type concentric bonding in the HOMO.

To further explore the nature of the interaction energy (E_{int}) between the endohedral atom and the cage, we performed the energy decomposition analysis (EDA) within the Morokuma−Ziegler scheme,[64−66] for leading to different chemically meaningful contributing terms according to

$$\Delta E_{int} = \Delta E_{orb} + \Delta E_{elstat} + \Delta E_{disp} + \Delta E_{Pauli}$$

Here,[65] stabilizing ΔE_{elstat} term refers to the electrostatic character of the interaction, which is obtained by considering each defined fragment (namely, A and B) in its unperturbed (frozen) electron density as isolated species ($\Psi_A\Psi_B$). Next, the repulsive ΔE_{Pauli} term accounts for the four-electron two-orbital interactions between occupied orbitals, which is calculated from the energy change in the process of antisymmetrization and renormalization of the overlapped fragment densities ($\Psi_0 = N\hat{A}\{\Psi_A\Psi_B\}$). Finally, stabilizing ΔE_{orb} term obtained when the densities of the constituent fragments relax into the final molecular orbitals (Ψ_{AB}) accounts for the covalent character of the interaction. In addition, the pairwise correction of Grimme[67] (DFT-D3) allows us to evaluate the dispersion interaction (ΔE_{disp}) related to London forces. To overcome basis set superposition error (BSSE), the counterpoise method was employed.

The relative contribution of the stabilizing terms given for the Au(I) + $[Au_{24}(SR)_{18}]^{2-} \rightarrow [Au@Au_{24}(SR)_{18}]^{-}$ and E(IV) + $[Au_{24}(SR)_{18}]^{2-} \rightarrow [E@Au_{24}(SR)_{18}]^{2+}$ processes, given by ΔE_{orb}, ΔE_{elstat}, and ΔE_{disp}, accounts for the overall character of the interaction. For the series, the ΔE_{disp} term contributes in a smaller extent, in the range from 0.3 to 2.1% of the overall stabilizing terms. In $[Au@Au_{24}(SMe)_{18}]^{-}$, the interaction exhibits an electrostatic character (63.4%), with a lower amount (34.5%) of covalent character. Interestingly, for the group XIV endohedrals, the covalent character becomes more relevant in agreement to the s- and p-type bonding interactions depicted above versus the single s-type interaction in the gold counterpart. Going down in the group, the covalent character decreases from 75.9 to 66.8%, due to the contribution from the 5d-block

The ΔE_{orb} term can be further studied through the energy decomposition analysis with natural orbitals for chemical valence[68−70] (EDA-NOCV). The inspection of the deformation densities from the NOCV analysis depicting the in- and out-flow of charges between the E(IV) and $[Au_{24}(SR)_{18}]^{2-}$ fragments reveals characteristic patterns for concentric s- and p-type bonding interactions. As representative example, the relevant deformation densities for $[Sn@Au_{24}(SR)_{18}]^{2+}$ are given on Figure 4.

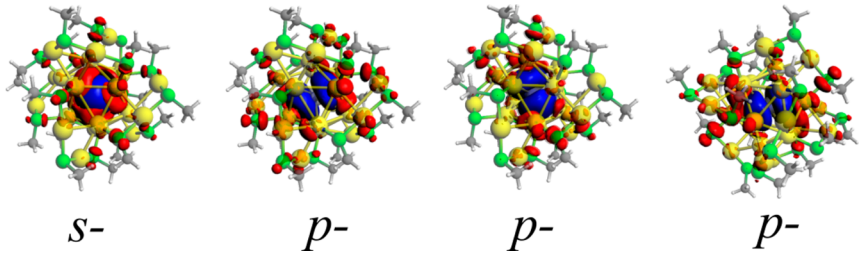

Figure 4. Deformation densities obtained from the natural orbital for chemical valence approach, accounting for s- and p-type bonding interactions for $[Sn@Au_{24}(SMe)_{18}]^{2+}$. See Table 3.

DOI: 10.1021/acs.jpcc.6b04943
J. Phys. Chem. C 2016, 120, 27019−27026

Table 3. Results from Energy Decomposition Analysis with Natural Orbitals for Chemical Valence (EDA-NOCV) Accounting for s- and p-Type Interactions[a]

@	Au		Si		Ge		Sn		Pb	
s-type	−62.6	6.9%	−406.7	24.3%	−485.7	29.8%	−361.6	26.0%	−477.2	33.7%
p*x*-type	−21.8	2.4%	−237.8	14.2%	−226.7	13.9%	−198.1	14.2%	−180.3	12.7%
p*y*-type	−21.8	2.4%	−246.1	14.7%	−215.9	13.2%	−186.7	13.4%	−167.1	11.8%
p*z*-type	−21.8	2.4%	−216.5	12.9%	−211.2	13.0%	−171.2	12.3%	−165.3	11.7%
R_{est}	−778.1	85.9%	−568.3	33.9%	−490.3	30.1%	−472.7	34.0%	−428.0	30.2%

[a]Values in kcal·mol^{-1}. In addition, the percent contribution to the overall orbital energetic term is given.

The associated stabilization energy for the s- and p-type interactions are given on Table 3. For Au, the s-type interaction contributes with −62.6 kcal·mol^{-1} to the overall ΔE_{orb} term (6.9%), followed by −21.8 kcal·mol^{-1} per each p-type interaction involving a charge donation to the 6p-Au atomic orbital (2.4% each). The remainder contribution to ΔE_{orb} (−778.1 kcal·mol^{-1}) is given by several smaller terms.

In Si, the stabilization from the s-type interaction raises up to −406.7 kcal·mol^{-1}, accounting for 24.3% of the orbital interaction, which is larger for Ge (−485.7 kcal·mol^{-1}, 29.8%) and Pb (−477.2 kcal·mol^{-1}, 33.7%). For Sn, the contribution to the stabilization decreases to −361.6 (26%). Thus, the order Ge > Pb > Si > Sn is found for the stabilizing s-type interaction, which agrees with the stabilization of the 1s superatomic orbital of the overall $[E@Au_{24}(SR)_{18}]^{2+}$ structure (Figure 3). The p-type interaction is more relevant for the group XIV endohedrals, which rises from −21.8 to about −200 kcal·mol^{-1} (~14% of ΔE_{orb}) from the Au to E (E = Si, Ge, Sn, and Pb) counterparts. The contribution decreases going down in the group, suggesting that a larger participation of E to HOMO (*vide infra*) leads to a lesser stabilization of such interaction.

The optical properties of gold nanoclusters provides useful information in explorative synthesis, allowing a initial characterization prior to mass and X-ray analysis.[23] In order to unravel possible characteristic patterns for group XIV endohedral counterparts, we calculated their optical absorption spectra (Figure 5). As has been discussed previously, $[Au@Au_{24}(SR)_{18}]^{-}$ exhibits a first low-energy electronic transitions involving both HOMO and LUMO, which is ascribed to a 1p → 1d transition (Table 4). Such transition is calculated at 1.41 eV, consistent with recent theoretical analysis.[36] The second peak observed at 2.19 depicts a combined 1p → 1d and "5d-Au block" → 1d transition and a third peak at 2.49 eV with a main "5d-Au block" → 1d character.

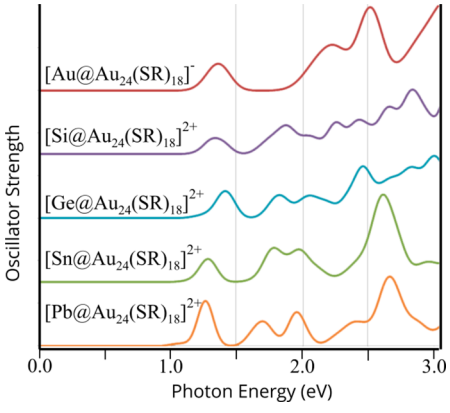

Figure 5. Calculated low-energy absorption spectra for for $[Au@Au_{24}(SMe)_{18}]^{-}$ and $[E@Au_{24}(SMe)_{18}]^{2+}$ (E = Si, Ge, Sn, and Pb), as obtained from SR calculations.

For $[E@Au_{24}(SMe)_{18}]^{2+}$, several features are observed in the low-energy region. In comparison to the gold counterpart, two extra peaks are described between 1.5 and 2.0 eV, which are of 1p → 1d and "5d-Au block" → 1d character, with a lesser contribution of a 1p → 2s transition. In overall, we found that the 1p → 1d transition is more allowed than the respective 1p → 2s, by comparing the dipole transition moment generated for a single transition of about 1.30 au and 0.05 au, respectively.

A detailed analysis of the calculated absorption spectra (Table 3) reveals that for the systems with 2s located close to the 2-fold part of the 1d superatomic shell, namely, Ge and Pb, the first peak exhibits a combined 1p → 1d and 1p → 2s character, whereas for Si and Sn, the second peak compromise the 1p → 2s transition. In addition, the calculated optical spectrum of $[C@Au_{24}(SR)_{18}]^{2+}$ is given in the Supporting Information, displaying a different peak pattern owing to the large distortion of the $C@Au_{12}$ core (see above).

The inclusion of the spin−orbit coupling causes the splitting of the atomic levels with $l > 0$, due to coupling of l and s for each electron. In this sense, total-angular momenta j ($j = l \pm s$) are employed to designate the atomic or superatomic spinors, instead of the pure orbital angular momentum (l) atomic orbital representation. This effect has been accounted for the 18-ve cluster $W@Au_{12}$,[71−74] among other superatomic clusters,[63,75] where the $1p^6$ and $1d^{10}$ superatomic shells splits into $1p_{1/2}^2 \oplus 1p_{3/2}^4$ and $1d_{3/2}^4 \oplus 1d_{5/2}^6$, respectively.

Consequently, the electronic configuration for $[Au@Au_{24}(SR)_{18}]^{-}$, given by $1s^2\ 1p^6$, can be depicted as $1s_{1/2}^2\ 1p_{1/2}^2\ 1p_{3/2}^4$, under the spin−orbit regime (Figure 6), leading to a splitting of $\xi_{SO}^{1p} = 0.17$ eV (spin−orbit constant) for the p-shell. Jiang and co-workers[36] have shown the consequences on the absorption spectrum for the spin−orbit effect on such cluster, resulting in a splitting of the first 1p→ 1d peak, due to the presence of $1p_{1/2}$ → 1d and $1p_{3/2}$ → 1d transitions.

The optical spectrum under the spin−orbit coupling (Figure 7) is consequently ruled by the new selection rules raised by the use of superatomic spinors, instead of pure orbital representations.[45,76,77] The comparison between the dipole allowed transitions is given on Table 5, which are generated in terms of superatomic orbitals. In the scenario neglecting the spin−orbit coupling, a 1p → 1d and 1p → 2s transition leads to electric dipole (μi, with $i = x, y, z$) symmetry allowed transitions with a polarization compromising the three axis ($\mu_{x,y,z}$). For transitions from $1p_{1/2}$ and $1p_{3/2}$ toward $1d_{3/2}$, $1d_{5/2}$, or $2s_{1/2}$, different polarizations are allowed (Table 5).

The $1p^6$ HOMO for the studied series splits into $1p_{1/2}^2 \oplus 1p_{3/2}^4$, separated by 0.16 eV ($\xi_{SO}^{1p}$) for silicon, which is latter reduced along the series due to a trend to shift the order to $1p_{3/2}^4 \oplus 1p_{1/2}^2$, as observed for Sn counterpart. As result, for

DOI: 10.1021/acs.jpcc.6b04943
J. Phys. Chem. C 2016, 120, 27019−27026

Table 4. Dipole Allowed Transition and the Respective Oscillator Strength (f) for the Studied Clusters Obtained at the Scalar Relativistic Level of theory

	E (eV)	f	character
	1.41	0.063	1p → 1d
$[Au_{25}(SMe)_{18}]^-$	2.19	0.108	1p → 1d + "5d-Au block" → 1d
	2.49	0.196	"5d-Au block" → 1d
	1.32	0.037	1p → 1d
$[Si@Au_{24}(SMe)_{18}]^{2+}$	1.87	0.068	1p → 1d + 1p → 2s
	2.04	0.043	1p → 1d
	1.41	0.064	1p → 1d + 1p → 2s
$[Ge@Au_{24}(SMe)_{18}]^{2+}$	1.82	0.054	1p → 1d
	2.05	0.053	1p → 1d
	1.28	0.054	1p → 1d
$[Sn@Au_{24}(SMe)_{18}]^{2+}$	1.79	0.080	1p → 1d + 1p → 2s
	1.97	0.076	1p → 1d
	1.24	0.105	1p → 1d + 1p → 2s
$[Pb@Au_{24}(SMe)_{18}]^{2+}$	1.68	0.059	1p → 1d
	1.94	0.079	1p → 1d

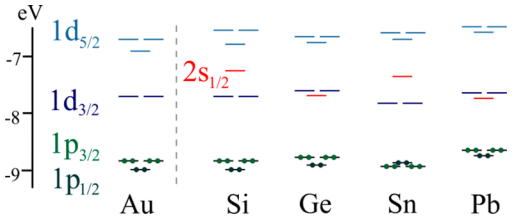

Figure 6. Frontier electronic structure for $[Au@Au_{24}(SMe)_{18}]^-$ and $[E@Au_{24}(SMe)_{18}]^{2+}$ (E = Si, Ge, Sn, and Pb) denoting the respective superatomic shells according under the spin−orbit coupling regime.

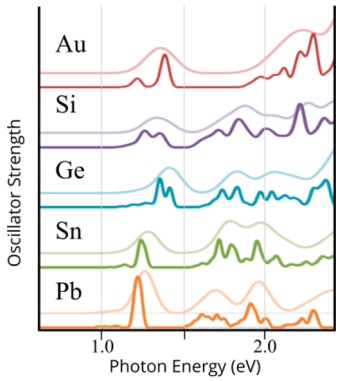

Figure 7. Calculated low-energy absorption spectra for for $[Au@Au_{24}(SMe)_{18}]^-$ and $[E@Au_{24}(SMe)_{18}]^{2+}$ (E = Si, Ge, Sn, and Pb), as obtained from spin−orbit calculations. For comparison, the obtained spectrum neglecting SOC is given in the background.

Table 5. Comparison of the Selection Rules for Dipole Allowed Transitions in Terms of Superatomic Orbitals[a]

	SR		
→	2s	1d	
1p	$\mu_{x,y,z}$	$\mu_{x,y,z}$	
	SOC		
→	$2s_{1/2}$	$1d_{3/2}$	$1d_{5/2}$
$1p_{3/2}$	$\mu_{x,y}$	μ_z	$\mu_{x,y,z}$
$1p_{1/2}$	$\mu_{x,y,z}$	$\mu_{x,y}$	$\mu_{x,y,z}$

[a]Scalar relativistic (SR) and spin-orbit (SOC) relativistic level of theory are shown.

Ge, Sn, and Pb, the ξ_{SO}^{1p} is calculated to be 0.13, 0.07, and 0.08 eV.

Similarly to the absorption spectrum calculated by Jiang and co-workers, taking into account the SOC, for the studied series the splitting of related peaks is also observed. In Figure 7, the spectrum at both scalar relativistic (SR, neglecting SOC) and SOC levels are compared, where the first peak splits into two peaks. This is more pronounced for the Au, Si, and Ge counterparts, where ξ_{SO}^{1p} ranges from 0.17 to 0.13 eV. For Sn and Pb, such peaks coalesce into a single one owing to the smaller ξ_{SO}^{1p} depicted above. In addition, transitions involving the 1p superatomic shells, also split as can be observed for the second peak described from SR calculations.

CONCLUSIONS

The optical properties of a series derived from relevant gold nanoparticles given by $Au_{25}(SR)_{18}$ can be tuned efficiently by varying the nature of the central atom. By moving from Au to a p-block endohedral element (E = Si, Ge, Sn, and Pb), a variation of the absorption spectrum is estimated by the modification of frontier levels, owing to the contribution from the novel 1p → 2s transition. Thus, a characteristic pattern owing to the variation of optical properties is expected. The bonding in the p-block endohedral structures shows an extension to the regular s-type interaction observed in $[Au@Au_{24}(SR)_{18}]^-$, leading to a more extended and covalent interaction involving effectively both of s- and p- shells, which can be expected to other endohedral p-block elements. This can be a useful approach in the fine-tuning of such properties, revealing the role of the p-elements into the frontier levels and bonding and optical properties. Moreover, the inclusion of the spin−orbit coupling modifies the absorption spectrum, resulting in a different variation between the studied series. The characteristic optical and bonding patterns resulting from the p-element doping of superatoms, as given here, shed light into the variation of the molecular properties according to the involved atom as an endohedral doping element.

ASSOCIATED CONTENT

Supporting Information

The Supporting Information is available free of charge on the ACS Publications website at DOI: 10.1021/acs.jpcc.6b04943.

DOI: 10.1021/acs.jpcc.6b04943
J. Phys. Chem. C 2016, 120, 27019−27026

Distortion of the C@Au_{12} core in $[C@Au_{24}(SMe)_{18}]^{2+}$ and the corresponding calculated optical spectrum (PDF)

AUTHOR INFORMATION

Corresponding Author

*E-mail: alvaro.munoz@uautonoma.cl.

ORCID

Alvaro Muñoz-Castro: 0000-0001-5949-9449

Notes

The authors declare no competing financial interest.

ACKNOWLEDGMENTS

We thank the reviewers for their useful comments. This work was supported by FONDECYT 1140359 and MILLENNIUM PROJECT RC120001 grants.

REFERENCES

(1) Qian, H.; Zhu, Y.; Jin, R. Size-Focusing Synthesis, Optical and Electrochemical Properties of Monodisperse $Au_{38}(SC_2H_4Ph)_{24}$ Nanoclusters. *ACS Nano* **2009**, *3*, 3795−3803.

(2) Whetten, R. L.; Khoury, J. T.; Alvarez, M. M.; Murthy, S.; Vezmar, I.; Wang, Z. L.; Stephens, P. W.; Cleveland, C. L.; Luedtke, W. D.; Landman, U. Nanocrystal Gold Molecules. *Adv. Mater.* **1996**, *8*, 428−433.

(3) Oro, L. A.; Braunstein, P.; Raithby, P. R. *Metal Clusters in Chemistry*; Wiley: Weinheim, Germany, 1999; Vol. 3.

(4) Daniel, M.-C.; Astruc, D. Gold Nanoparticles: Assembly, Supramolecular Chemistry, Quantum-Size-Related Properties, and Applications toward Biology, Catalysis, and Nanotechnology. *Chem. Rev.* **2004**, *104*, 293−346.

(5) Heaven, M. W.; Dass, A.; White, P. S.; Holt, K. M.; Murray, R. W. Crystal Structure of the Gold Nanoparticle $[N(C_8H_{17})_4][Au_{25}(SCH_2CH_2Ph)_{18}]$. *J. Am. Chem. Soc.* **2008**, *130*, 3754−3755.

(6) Walter, M.; Akola, J.; Lopez-Acevedo, O.; Jadzinsky, P. D.; Calero, G.; Ackerson, C. J.; Whetten, R. L.; Grönbeck, H.; Häkkinen, H. A Unified View of Ligand-Protected Gold Clusters as Superatom Complexes. *Proc. Natl. Acad. Sci. U. S. A.* **2008**, *105*, 9157−9162.

(7) Jena, P. Beyond the Periodic Table of Elements: The Role of Superatoms. *J. Phys. Chem. Lett.* **2013**, *4*, 1432−1442.

(8) Knoppe, S.; Dolamic, I.; Bürgi, T. Racemization of a Chiral Nanoparticle Evidences the Flexibility of the Gold-Thiolate Interface. *J. Am. Chem. Soc.* **2012**, *134*, 13114−13120.

(9) Levi-Kalisman, Y.; Jadzinsky, P. D.; Kalisman, N.; Tsunoyama, H.; Tsukuda, T.; Bushnell, D. A.; Kornberg, R. D. Synthesis and Characterization of $Au_{102}(P\text{-}MBA)_{44}$ Nanoparticles. *J. Am. Chem. Soc.* **2011**, *133*, 2976−2982.

(10) Galloway, J. M.; Bramble, J. P.; Rawlings, A. E.; Burnell, G.; Evans, S. D.; Staniland, S. S. Biotemplated Magnetic Nanoparticle Arrays. *Small* **2012**, *8*, 204−208.

(11) Tsukuda, T.; Tsunoyama, H.; Sakurai, H. Aerobic Oxidations Catalyzed by Colloidal Nanogold. *Chem. - Asian J.* **2011**, *6*, 736−748.

(12) Zhu, Y.; Qian, H.; Jin, R. Catalysis Opportunities of Atomically Precise Gold Nanoclusters. *J. Mater. Chem.* **2011**, *21*, 6793−6799.

(13) Kwak, K.; Kumar, S. S.; Lee, D. Selective Determination of Dopamine Using Quantum-Sized Gold Nanoparticles Protected with Charge Selective Ligands. *Nanoscale* **2012**, *4*, 4240−4246.

(14) Sakai, N.; Tatsuma, T. Photovoltaic Properties of Glutathione-Protected Gold Clusters Adsorbed on TiO_2 Electrodes. *Adv. Mater.* **2010**, *22*, 3185−3188.

(15) Wu, Z.; Wang, M.; Yang, J.; Zheng, X.; Cai, W.; Meng, G.; Qian, H.; Wang, H.; Jin, R. Well-Defined Nanoclusters as Fluorescent Nanosensors: A Case Study on $Au_{25}(SG)_{18}$. *Small* **2012**, *8*, 2028−2035.

(16) Murray, R. W. Nanoelectrochemistry: Metal Nanoparticles, Nanoelectrodes, and Nanopores. *Chem. Rev.* **2008**, *108*, 2688−2720.

(17) Häkkinen, H. Atomic and Electronic Structure of Gold Clusters: Understanding Flakes, Cages and Superatoms from Simple Concepts. *Chem. Soc. Rev.* **2008**, *37*, 1847−1859.

(18) Zhu, M.; Aikens, C. M.; Hollander, F. J.; Schatz, G. C.; Jin, R. Correlating the Crystal Structure of a Thiol-Protected Au_{25} Cluster and Optical Properties. *J. Am. Chem. Soc.* **2008**, *130*, 5883−5885.

(19) Zhu, M.; Eckenhoff, W. T.; Pintauer, T.; Jin, R. Conversion of Anionic $[Au_{25}(SCH_2CH_2Ph)_{18}]^-$ Cluster to Charge Neutral Cluster via Air Oxidation. *J. Phys. Chem. C* **2008**, *112*, 14221−14224.

(20) Aikens, C. M. Effects of Core Distances, Solvent, Ligand, and Level of Theory on the TDDFT Optical Absorption Spectrum of the Thiolate-Protected Au_{25} Nanoparticle. *J. Phys. Chem. A* **2009**, *113*, 10811−10817.

(21) Aikens, C. M. Electronic Structure of Ligand-Passivated Gold and Silver Nanoclusters. *J. Phys. Chem. Lett.* **2011**, *2*, 99−104.

(22) Jiang, D. The Expanding Universe of Thiolated Gold Nanoclusters and Beyond. *Nanoscale* **2013**, *5*, 7149−7160.

(23) Jin, R. Atomically Precise Metal Nanoclusters: Stable Sizes and Optical Properties. *Nanoscale* **2015**, *7*, 1549−1565.

(24) Castleman, A. W.; Khanna, S. N. Clusters, Superatoms, and Building Blocks of New Materials. *J. Phys. Chem. C* **2009**, *113*, 2664−2675.

(25) Jadzinsky, P. D.; Calero, G.; Ackerson, C. J.; Bushnell, D. A.; Kornberg, R. D. Structure of a Thiol Monolayer-Protected Gold Nanoparticle at 1.1 {Å} Resolution. *Science* **2007**, *318*, 430−433.

(26) Claridge, S. A.; Castleman, A. W.; Khanna, S. N.; Murray, C. B.; Sen, A.; Weiss, P. S. Cluster-Assembled Materials. *ACS Nano* **2009**, *3*, 244−255.

(27) Toikkanen, O.; Ruiz, V.; Ronnholm, G.; Kalkkinen, N.; Liljeroth, P.; Quinn, B. M. Synthesis and Stability of Monolayer-Protected Au_{38} Clusters. *J. Am. Chem. Soc.* **2008**, *130*, 11049−11055.

(28) Qian, H.; Liu, C.; Jin, R. Controlled Growth of Molecularly Pure $Au_{25}(SR)_{18}$ and $Au_{38}(SR)_{24}$ Nanoclusters from the Same Polydispersed Crude Product. *Sci. China: Chem.* **2012**, *55*, 2359−2365.

(29) Maity, P.; Xie, S.; Yamauchi, M.; Tsukuda, T. Stabilized Gold Clusters: From Isolation toward Controlled Synthesis. *Nanoscale* **2012**, *4*, 4027−4037.

(30) Häkkinen, H. The Gold-Sulfur Interface at the Nanoscale. *Nat. Chem.* **2012**, *4*, 443−455.

(31) Khanna, S.; Jena, P. Assembling Crystals from Clusters. *Phys. Rev. Lett.* **1992**, *69*, 1664−1667.

(32) Reveles, J. U.; Khanna, S. N.; Roach, P. J.; Castleman, A. W. Multiple Valence Superatoms. *Proc. Natl. Acad. Sci. U. S. A.* **2006**, *103*, 18405−18410.

(33) Muñoz-Castro, A. Sp^3-Hybridization in Superatomic Clusters. Analogues to Simple Molecules Involving the Au_6 Core. *Chem. Sci.* **2014**, *5*, 4749−4754.

(34) Jiang, D.; Dai, S. From Superatomic $Au_{25}(SR)_{18}^-$ to Superatomic M@Au_{24} $(SR)_{18}$ Q Core- Shell Clusters. *Inorg. Chem.* **2009**, *48*, 2720−2722.

(35) Jung, J.; Kang, S.; Han, Y.-K. Ligand Effects on the Stability of Thiol-Stabilized Gold Nanoclusters: $Au_{25}(SR)_{18}^-$, $Au_{38}(SR)_{24}$, and $Au_{102}(SR)_{44}$. *Nanoscale* **2012**, *4*, 4206−4210.

(36) Jiang, D.; Kuhn, M.; Tang, Q.; Weigend, F. Superatomic Orbitals under Spin−Orbit Coupling. *J. Phys. Chem. Lett.* **2014**, *5*, 3286−3289.

(37) Lopez-Acevedo, O.; Tsunoyama, H.; Tsukuda, T.; Häkkinen, H.; Aikens, C. M. Chirality and Electronic Structure of the Thiolate-Protected Au_{38} Nanocluster. *J. Am. Chem. Soc.* **2010**, *132*, 8210−8218.

(38) Yao, C.; Lin, Y.; Yuan, J.; Liao, L.; Zhu, M.; Weng, L.; Yang, J.; Wu, Z. Mono-Cadmium vs Mono-Mercury Doping of Au_{25} Nanoclusters. *J. Am. Chem. Soc.* **2015**, *137*, 15350−15353.

(39) Christensen, S. L.; MacDonald, M. A.; Chatt, A.; Zhang, P.; Qian, H.; Jin, R. Dopant Location, Local Structure, and Electronic Properties of Au $_{24}Pt(SR)_{18}$ Nanoclusters. *J. Phys. Chem. C* **2012**, *116*, 26932−26937.

(40) Negishi, Y.; Munakata, K.; Ohgake, W.; Nobusada, K. Effect of Copper Doping on Electronic Structure, Geometric Structure, and

DOI: 10.1021/acs.jpcc.6b04943
J. Phys. Chem. C 2016, 120, 27019−27026

Stability of Thiolate-Protected Au25 Nanoclusters. *J. Phys. Chem. Lett.* **2012**, *3*, 2209−2214.
(41) Jin, R.; Nobusada, K. Doping and Alloying in Atomically Precise Gold Nanoparticles. *Nano Res.* **2014**, *7*, 285−300.
(42) Qian, H.; Jiang, D.; Li, G.; Gayathri, C.; Das, A.; Gil, R. R.; Jin, R. Monoplatinum Doping of Gold Nanoclusters and Catalytic Application. *J. Am. Chem. Soc.* **2012**, *134*, 16159−16162.
(43) Xie, S.; Tsunoyama, H.; Kurashige, W.; Negishi, Y.; Tsukuda, T. Enhancement in Aerobic Alcohol Oxidation Catalysis of Au_{25} Clusters by Single Pd Atom Doping. *ACS Catal.* **2012**, *2*, 1519−1523.
(44) Kwak, K.; Tang, Q.; Kim, M.; Jiang, D.; Lee, D. Interconversion between Superatomic 6-Electron and 8-Electron Configurations of $M@Au_{24}(SR)_{18}$ Clusters (M = Pd, Pt). *J. Am. Chem. Soc.* **2015**, *137*, 10833−10840.
(45) Dyall, K. G.; Fægri, K. *Introduction to Relativistic Quantum Chemistry*; Oxford University Press: New York, 2007.
(46) *Amsterdam Density Functional (ADF) Code*; Software for Chemistry & Materials (SCM): Amsterdam, The Netherlands, 2016. http://www.scm.com (accessed October 24, 2016).
(47) van Lenthe, E.; Baerends, E.-J. J.; Snijders, J. G. Relativistic Total Energy Using Regular Approximations. *J. Chem. Phys.* **1994**, *101*, 9783.
(48) Perdew, J. P.; Burke, K.; Wang, Y. Generalized Gradient Approximation for the Exchange-Correlation Hole of a Many-Electron System. *Phys. Rev. B: Condens. Matter Mater. Phys.* **1996**, *54*, 16533−16539.
(49) Perdew, J. P.; Burke, K.; Ernzerhof, M. Generalized Gradient Approximation Made Simple. *Phys. Rev. Lett.* **1997**, *78*, 1396−1396.
(50) Lopez-Acevedo, O.; Akola, J.; Whetten, R. L.; Gronbeck, H.; Häkkinen, H. Ha kkinen, H. Structure and Bonding in the Ubiquitous Icosahedral Metallic Gold Cluster $Au_{144}(SR)_{60}$. *J. Phys. Chem. C* **2009**, *113*, 5035−5038.
(51) Akola, J.; Walter, M.; Whetten, R. L.; Häkkinen, H.; Grönbeck, H. On the Structure of Thiolate-Protected Au_{25}. *J. Am. Chem. Soc.* **2008**, *130*, 3756−3757.
(52) Akola, J.; Kacprzak, K.; Lopez-Acevedo, O.; Walter, M.; Grönbeck, H.; Häkkinen, H. Thiolate-Protected Au_{25} Superatoms as Building Blocks: Dimers and Crystals. *J. Phys. Chem. C* **2010**, *114*, 15986−15994.
(53) Versluis, L.; Ziegler, T. The Determination of Molecular Structures by Density Functional Theory. The Evaluation of Analytical Energy Gradients by Numerical Integration. *J. Chem. Phys.* **1988**, *88*, 322−328.
(54) Ruiz-Martínez, A.; Casanova, D.; Alvarez, S. Polyhedral Structures with an Odd Number of Vertices: Nine-Coordinate Metal Compounds. *Chem. - Eur. J.* **2008**, *14*, 1291−1303.
(55) Cirera, J.; Ruiz, E.; Alvarez, S. Continuous Shape Measures as a Stereochemical Tool in Organometallic Chemistry. *Organometallics* **2005**, *24*, 1556−1562.
(56) Alvarez, S.; Alemany, P.; Casanova, D.; Cirera, J.; Llunell, M.; Avnir, D. Shape Maps and Polyhedral Interconversion Paths in Transition Metal Chemistry. *Coord. Chem. Rev.* **2005**, *249*, 1693−1708.
(57) Scherbaum, F.; Grohmann, A.; Huber, B.; Krüger, C.; Schmidbaur, H. Aurophilicity" as a Consequence of Relativistic Effects: The Hexakis(triphenylphosphaneaurio)methane Dication-$[(Ph_3PAu)_6C]_2^+$. *Angew. Chem., Int. Ed. Engl.* **1988**, *27*, 1544−1546.
(58) Schmidbaur, H. The Fascinating Implications of New Results in Gold Chemistry. *Gold Bull.* **1990**, *23*, 11−21.
(59) Steigelmann, O.; Bissinger, P.; Schmidbaur, H. Assembly of the$[CAu_6]_2^+$ Cluster with a Tailor-Made Diphosphane Spanning the Octahedral Edges. *Angew. Chem., Int. Ed. Engl.* **1990**, *29*, 1399−1400.
(60) Jia, J.-H.; Liang, J.-X.; Lei, Z.; Cao, Z.-X.; Wang, Q.-M. A Luminescent Gold(I)−copper(I) Cluster with Unprecedented Carbon-Centered Trigonal Prismatic Hexagold. *Chem. Commun.* **2011**, *47*, 4739.
(61) Hirshfeld, F. L. Bonded-Atom Fragments for Describing Molecular Charge Densities. *Theor. Chim. Acta* **1977**, *44*, 129−138.
(62) Wiberg, K. B.; Rablen, P. R. Comparison of Atomic Charges Derived via Different Procedures. *J. Comput. Chem.* **1993**, *14*, 1504−1518.
(63) Muñoz-Castro, A. Golden Endohedral Main-Group Clusters, $[E@Au_{12}]^{q-}$: Theoretical Insights Into the 20-e Principle. *J. Phys. Chem. Lett.* **2013**, *4*, 3363−3366.
(64) Morokuma, K. Molecular Orbital Studies of Hydrogen Bonds. III. C═O···H−O Hydrogen Bond in $H_2CO···H_2O$ and $H_2CO···2H_2O$. *J. Chem. Phys.* **1971**, *55*, 1236−1244.
(65) Te Velde, G.; Bickelhaupt, F. M.; Baerends, E. J.; Fonseca Guerra, C.; van Gisbergen, S. J. a.; Snijders, J. G.; Ziegler, T. Chemistry with ADF. *J. Comput. Chem.* **2001**, *22*, 931−967.
(66) Ziegler, T.; Rauk, A. On the Calculation of Bonding Energies by the Hartree Fock Slater Method. *Theor. Chim. Acta* **1977**, *46*, 1−10.
(67) Grimme, S. Density Functional Theory with London Dispersion Corrections. *Wiley Interdiscip. Rev. Comput. Mol. Sci.* **2011**, *1*, 211−228.
(68) Nalewajski, R. F.; Mrozek, J.; Michalak, A. Two-Electron Valence Indices from the Kohn-Sham Orbitals. *Int. J. Quantum Chem.* **1997**, *61*, 589−601.
(69) Michalak, A.; DeKock, R. L.; Ziegler, T. Bond Multiplicity in Transition-Metal Complexes: Applications of Two-Electron Valence Indices. *J. Phys. Chem. A* **2008**, *112*, 7256−7263.
(70) *The Chemical Bond: Fundamental Aspects of Chemical Bonding*; Frenking, G., Shaik, S., Eds.; Wiley-VCH Verlag GmbH & Co. KGaA: Weinheim, Germany, 2014.
(71) Pyykkö, P.; Runeberg, N. Icosahedral WAu_{12}: A Predicted Closed-Shell Species, Stabilized by Aurophilic Attraction and Relativity and in Accord with the 18-Electron Rule. *Angew. Chem., Int. Ed.* **2002**, *41*, 2174−2176.
(72) Li, X.; Kiran, B.; Li, J.; Zhai, H.-J.; Wang, L.-S. Experimental Observation and Confirmation of Icosahedral $W@Au_{12}$ and $Mo@Au_{12}$ Molecules. *Angew. Chem., Int. Ed.* **2002**, *41*, 4786−4789.
(73) Cao, G.-J.; Schwarz, W. H. E.; Li, J. An 18-Electron System Containing a Superheavy Element: Theoretical Studies of $Sg@Au_{12}$. *Inorg. Chem.* **2015**, *54*, 3695−3701.
(74) Muñoz-Castro, A.; Arratia-Perez, R. Spin−Orbit Effects on a Gold-Based Superatom: A Relativistic Jellium Model. *Phys. Chem. Chem. Phys.* **2012**, *14*, 1408−1411.
(75) Muñoz-Castro, A.; Mac-Leod Carey, D.; Arratia-Pérez, R. Inside a Superatom: The M_7^q (M = Cu, Ag, q = 1+, 0, 1-) Case. *ChemPhysChem* **2010**, *11*, 646−650.
(76) Muñoz-Castro, A.; MacLeod Carey, D.; Arratia-Pérez, R. Calculated Molecular Properties of Triangular Tribenzo and Perfluoro-Tribenzo Trimercuronin Macrocycles. *J. Phys. Chem. A* **2010**, *114*, 666−672.
(77) Muñoz-Castro, A.; Mac-Leod Carey, D.; Arratia-Pérez, R. Electronic Structure, Molecular Properties and Electronic Currents of the Luminescent $[Au_3(CH_3NCOCH_3)_3]$ Cluster. *Chem. Phys. Lett.* **2009**, *474*, 290−293.

DOI: 10.1021/acs.jpcc.6b04943
J. Phys. Chem. C 2016, 120, 27019−27026